FULL PAPER

Hard Radiation Detection from the Selenophosphate $Pb_2P_2Se_6$

*Peng L. Wang, Zhifu Liu, Pice Chen, John A. Peters, Gangjian Tan, Jino Im, Wenwen Lin, Arthur J. Freeman, Bruce W. Wessels, and Mercouri G. Kanatzidis**

The heavy metal selenophosphate, $Pb_2P_2Se_6$, is a promising new material for cost-effective X-ray/γ-ray detection. Crystal boules of $Pb_2P_2Se_6$ up to 25 mm in length and 15 mm in diameter are grown by a vertical Bridgman method. They are cut and processed into size-appropriate wafers for physical, phototransport property studies, as well as γ-ray detector testing. The material is a semiconductor with an indirect bandgap of 1.88 eV and has electrical resistivity in the range of 1×10^{10} Ω cm. $Pb_2P_2Se_6$ single crystal samples display a significant photoconductivity response to optical, X-ray, and γ-ray radiation. When tested with a ^{57}Co γ-ray source, $Pb_2P_2Se_6$ crystals show spectroscopic response and several generated pulse height spectra resolving the 122.1 and 136.5 keV ^{57}Co radiation. The mobility–lifetime product of $Pb_2P_2Se_6$ is estimated to be $\approx 3.5 \times 10^{-5}$ cm^2 V^{-1} for electron carriers. The $Pb_2P_2Se_6$ compound melts congruently at 812 °C and has robust chemical/physical properties that promise low cost bulk production and detector development.

1. Introduction

Room-temperature semiconducting X-ray/γ-ray detectors are crucial in a number of technologies, including biomedical imaging, national security, and spectroscopy instrumentation; however, the high cost of today's commercial detectors severely limits their broad application.[1] Finding low cost room-temperature radiation detectors is a complex, multifaceted challenge. First of all, there is a limited number of potential detector materials due to the low availability of heavy element compounds possessing suitable optical bandgaps (1.5–3.0 eV) and high resistivity. For example, the heavy chalcogenides, HgQ (Q = Se and Te), which are isostructural to CdTe and the rock salt PbQ, possess nearly zero or very narrow energy gaps.[2] The second problem arises from the complex physics and chemistry of compound semiconductors in comparison to their elemental counterparts such as Si and Ge. Third, many compounds with attractive bulk physical properties, such as α-HgS and TlI, exhibit phase transitions hindering the growth of high-quality single crystals.[3] For compounds suitable for crystal growth, e.g., the commercial benchmark $Cd_{0.9}Zn_{0.1}Te$ (CZT) detector material suffers from stoichiometric imbalance and Te phase precipitation rooted in its intrinsic chemical properties which prevent its low cost production.[1b,4]

Thanks to the rapid progress in solid state synthesis and compound discovery, our knowledge of novel semiconductor compounds and their chemical/physical properties has drastically expanded in the last two decades. In recent years, our group has investigated a number of heavy element, wide bandgap semiconductor compounds as potential hard radiation detection materials.[5] Many of these studies were inspired by the concept of "dimensional reduction" and lattice hybridization[2, 6] where binary semiconductors with high mass density and narrow bandgaps were combined with ones with wide bandgaps to form ternary materials with suitable bandgaps and high densities. In an alternative approach, the challenge in developing new radiation detectors can be alleviated by expanding the pool of potential detector materials to comprise heavy element chemical systems incorporating light *p*-block elements, such as Si and P. The higher electronegativity contrast brought by the light elements can lead to more desirable electronic structures (especially larger bandgaps) in these compounds without significantly compromising their high mass density.

Our group's experience with chalcophosphate chemistry[7] has led us to identify lead chalcophosphate compounds in general, and $Pb_2P_2Q_6$ (Q = S, Se)[8] in particular as promising semiconductors for hard radiation detection. The two isostructural $Pb_2P_2Q_6$ compounds crystallize in the $P2_1/c$ space group with a = 6.606 Å, b = 7.464 Å, c = 11.346 Å, β = 124.10° for $Pb_2P_2S_6$, and a = 6.910 Å, b = 7.670 Å, c = 11.816 Å, β = 124.35° for $Pb_2P_2Se_6$.[8] As illustrated in **Figure 1**, the $Pb_2P_2Se_6$ is a salt of Pb^{2+} cations with the ethane like $[P_2Se_6]^{4-}$ anions. The $Pb_2P_2S_6$ and $Pb_2P_2Se_6$ display yellow and dark red color, respectively, reflecting their large optical bandgaps. Although both $Pb_2P_2S_6$ and $Pb_2P_2Se_6$ have attractive optical properties, the selenide with an average atomic number (Z) of 39.8 and a density of 6.14 g cm^{-3}[9] is

Dr. P. L. Wang, Dr. G. Tan, Dr. W. Lin,
Prof. M. G. Kanatzidis
Department of Chemistry
Northwestern University
Evanston, IL 60208, USA
E-mail: m-kanatzidis@northwestern.edu
Dr. Z. Liu, Dr. P. Chen, Dr. J. A. Peters, Prof. B. W. Wessels
Department of Materials Science and Engineering
Northwestern University
Evanston, IL 60208, USA
Dr. J. Im, Prof. A. J. Freeman
Department of Physics and Astronomy
Northwestern University
Evanston, IL 60208, USA

DOI: 10.1002/adfm.201501826

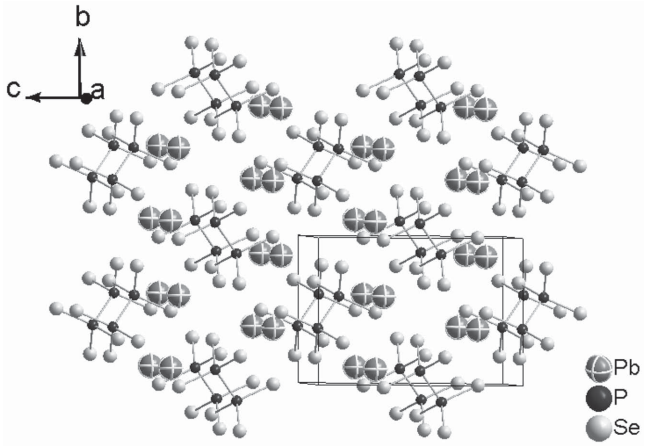

Figure 1. Crystal structure of $Pb_2P_2Se_6$.

certainly more suitable for high-energy X-ray and γ-ray applications. Figure S1 (Supporting Information) shows the attenuation length of $Pb_2P_2Se_6$ and CZT calculated using the atomic attenuation coefficients tabulated by the National Institute of Standards and Technology.[10] The attenuation coefficient of $Pb_2P_2Se_6$ is greater than that of CZT, especially at the high energy region, which relaxes, to some extent, the requirement of high mobility–lifetime product ($\mu\tau$) for an effective γ-ray detector. For example, for ^{137}Cs radiation at 662 keV, the attenuation length is 2.3 cm for CZT and only 1.8 cm for $Pb_2P_2Se_6$. In this case, the necessary distance for the charge carriers to travel to the electrodes is shorter in a $Pb_2P_2Se_6$ detector reducing the probability of trapping.

In addition to its bulk physical properties, another attractive feature of $Pb_2P_2Se_6$ as a detector material is its potential for low cost production. Compared to the commercial benchmark, CZT, an alloy of cadmium telluride and zinc telluride,[11] the stoichiometric ternary compound, $Pb_2P_2Se_6$, with its simpler phase diagram,[12] promises less technological and engineering challenges in terms of crystal growth and scale-up development. More importantly, the three elements of $Pb_2P_2Se_6$, namely, lead metal, red phosphorous, and selenium, are abundant and widely used, while their robust chemical and physical properties allow them to be easily extracted, isolated, and purified. The availability of high purity starting materials implies less complicated purification processes.

Based on the above-discussed properties, we have identified $Pb_2P_2Se_6$ as a potential cost-effective hard radiation detector material. In this work, we present the crystal growth, optical and electrical properties, as well as promising γ-ray response of the $Pb_2P_2Se_6$ single crystals. Other physical properties of this compound, such as thermal behavior and mechanical properties are also discussed with respect to its potential as a low cost detector material.

2. Results and Discussion

2.1. Synthesis, Crystal Growth, and Process

The $Pb_2P_2Se_6$ compound was prepared from as-purchased commercial elements without any further purification. The samples for exploratory crystal growth experiments and bulk physical property measurements (thermal, hardness) were prepared from lower purity starting materials (99.99%, wt), while the samples subjected to electrical measurements and γ-ray detection tests were grown from high purity elements (99.999%+, wt). As starting materials, lead metal, red phosphorus, and elemental selenium are chemically robust and physically stable substances, so they can be handled in the ambient environment. Although no additional purification was performed on the commercial starting materials other than the removal of the surface oxide on the lead rods, we have taken great care during the sample preparation to minimize the materials' exposure to possible sources of impurities such as surfaces and containers. Following the same guideline, the synthesis and crystal growth of $Pb_2P_2Se_6$ were performed in one single ampoule to reduce the chance of contamination.

Studies of $Pb_2P_2Se_6$ for other applications have demonstrated the growth of large single crystals by the Bridgman method.[13] The $Pb_2P_2Se_6$ compound exhibits a rather high melting point at 798 °C,[12] which creates a challenge for Bridgman crystal growth in terms of maintaining stable temperature zones. A high-temperature two-zone furnace was selected for the Bridgman growth in order to achieve the desired temperature stability. Because of the relatively short zones of our furnace (hot and cold zones were 125 mm long), a large thermal stress was created when the bottom of the crystal started to quickly cool down as it moves out of the heated part of the cold zone (see Figure S2, Supporting Information for the temperature profile). Such a situation is more pronounced when growing longer crystal ingots (>100 mm). As shown in **Figure 2**a, the

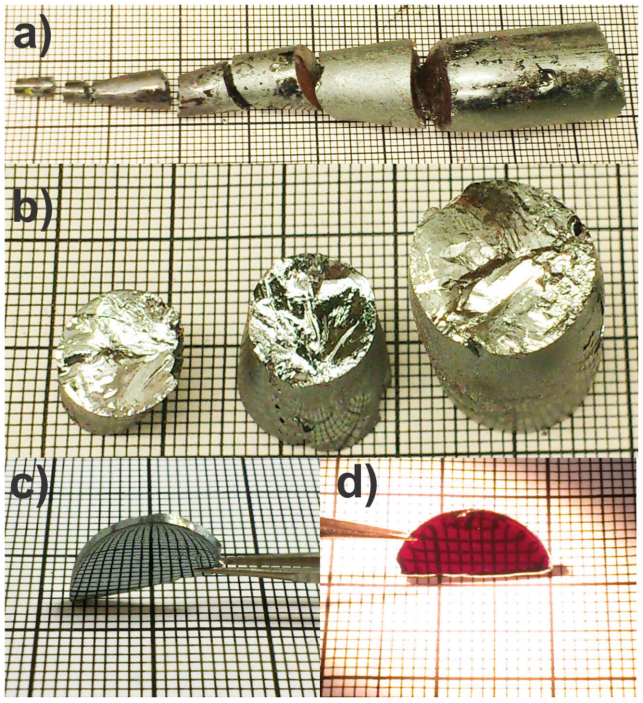

Figure 2. a) Whole $Pb_2P_2Se_6$ crystal ingot naturally fractured due to thermal stress (perpendicular to the growth direction). b) Large crack-free crystalline segments of $Pb_2P_2Se_6$ obtained from Bridgman growth. A polished $Pb_2P_2Se_6$ single crystal wafer c) under ambient light and d) under intense incandescent light.

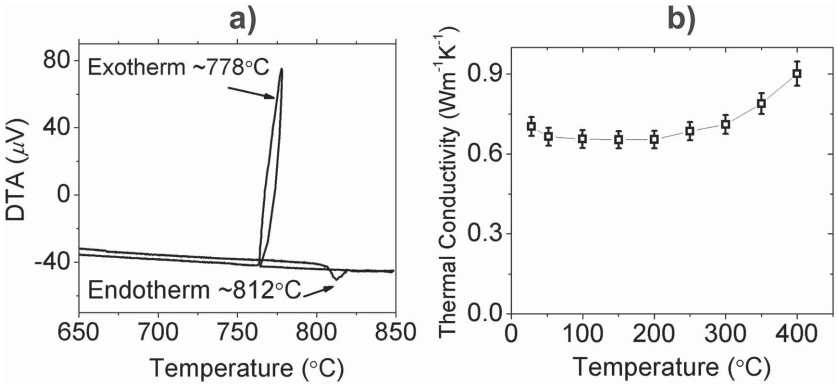

Figure 3. a) Differential thermal analysis of $Pb_2P_2Se_6$ between 600 and 800 °C, measured at a rate of 1 °C min^{-1}. b) Thermal conductivity of $Pb_2P_2Se_6$ up to 400 °C, measured at a rate of 1 °C min^{-1}.

large thermal stress caused multiple cleavages perpendicular to the growth direction. These cleavages are spaced closer to the bottom of the ingot indicating a greater temperature change toward the bottom the furnace.

The above-discussed crystal growth process yielded sizable, crack-free segments of crystal ingots (Figure 2b) with good reproducibility. These ingots were subsequently cut and polished into detector samples (see Figure S3, Supporting Information for multiple detector samples). As illustrated in Figure 2c,d, a $Pb_2P_2Se_6$ single crystal wafer less than 1 mm thick appeared transparent under intense incandescent light. When examined under polarized light, the sample exhibited uniform color change upon rotation (Figure S4a,b, Supporting Information), illustrating its single crystalline nature.

2.2. Thermal and Mechanical Properties

Although the crystal growth technique was simple at this stage, we were able to produce sizable, high quality crystal ingots of $Pb_2P_2Se_6$ because of its well-behaved thermal properties. The differential thermal analysis (DTA) performed on the polycrystalline $Pb_2P_2Se_6$ sample revealed only one endothermic peak at 812 °C and one exothermic peak at 778 °C (**Figure 3**a), indicating a congruent melting behavior (see Figure S5a, Supporting Information for the full, two heat/cool cycle DTA analysis). The discrepancy between the DTA data and the reported melting point[12] is likely caused by the fast heating and cooling rate (1 °C min^{-1}) used during the DTA analysis. The intense and sharp exothermic peak observed at 778 °C implies the $Pb_2P_2Se_6$ system favors a highly crystalline form upon solidification. As a result, during the crystal growth process, a large amount of heat needs to be conducted away from the liquid–solid interface through the just-formed crystalline material.

We have measured the thermal conductivity of an as-grown $Pb_2P_2Se_6$ single crystal along the growth direction up to 400 °C (Figure 3b, for heat capacity and thermal diffusivity see Figure S5b, Supporting Information). It is worth noting that the $Pb_2P_2Se_6$ exhibits an almost temperature-independent thermal conductivity between room temperature and 300 °C, in agreement with earlier measurements.[14] At temperatures above 300 °C, the thermal conductivity of $Pb_2P_2Se_6$ increases slightly with rising temperature. At 400 °C, the thermal conductivity of $Pb_2P_2Se_6$ is 0.90 ± 0.05 W m^{-1} K^{-1}, which is comparable to that of CZT (1 W m^{-1} K^{-1})[15] and higher than that of TlBr (0.52 W m^{-1} K^{-1}).[16] With a further improved Bridgman technique, the higher thermal conductivity of $Pb_2P_2Se_6$ in combination with its congruent melting behavior promises better single crystal yield and faster growth speeds, which are highly desirable material attributes for cost-effective bulk crystal production.

Another attractive property of a $Pb_2P_2Se_6$ crystal is its mechanical hardness. For soft materials, waferization and mechanical polishing performed during detector fabrication could introduce more defects that deteriorate its performance.[11] Microindentation measurements revealed a Knoop hardness of 106 ± 3 kg mm^{-2} for $Pb_2P_2Se_6$ (Figure S6, Supporting Information), which is significantly harder than CZT (60–80 kg mm^{-2})[1b,17] and TlBr (12 kg mm^{-2}).[1b,18] The superior hardness suggests that simpler postgrowth processes and device fabrication methods can be implemented for the future development of $Pb_2P_2Se_6$.

2.3. Optical Properties and Electronic Structure Calculations

The optical bandgap of $Pb_2P_2Se_6$ was determined to be 1.88 eV by UV–vis diffuse reflectance spectroscopy using ground crystals (Figure S7, Supporting Information).[5a] The observed optical bandgap of $Pb_2P_2Se_6$ was found in agreement with the ≈2 eV indirect bandgap predicted by the electronic structure calculations (**Figure 4**a). Interestingly, our theoretical calculations also revealed dominant contributions of Pb and Se based orbitals to the density of state (DOS, Figure 4b–d) at the vicinity of the Fermi level. Although the tetravalent phosphorus atoms play a limited role in the direct Pb—Se bonds, they produce strong covalent P—Se bonding in the $[P_2Se_6]^{4-}$ cluster, which in turn modulates Pb—Se bond strength to define the observed large bandgap.

2.4. Electronic Transport and Detector Properties

The room temperature electrical resistivity of $Pb_2P_2Se_6$ is of the order of 1×10^{10} Ω cm. This value is comparable to CZT and well above the threshold requirement of 10^8–10^9 Ω cm for effective room temperature γ-ray detector materials. With such a high resistivity, a $Pb_2P_2Se_6$ detector is expected to exhibit low dark current, so that higher bias can be applied to increase detector resolution and decrease readout time.

In addition to the high resistivity, when the $Pb_2P_2Se_6$ samples were subjected to 40 kV/10 mA Ag X-ray radiation, they produced a threefold increase in current under a 400 V bias (**Figure 5**). This observation illustrates the good photoconductivity properties of $Pb_2P_2Se_6$ under hard radiation.

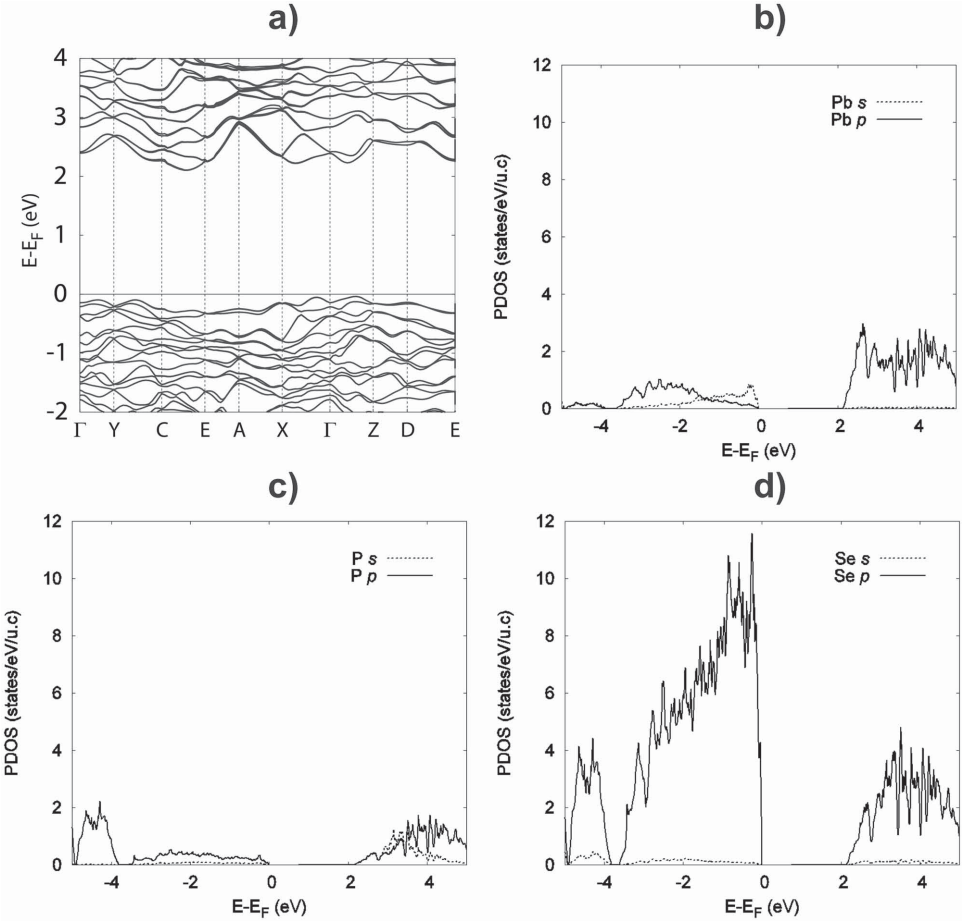

Figure 4. a) Electronic band structure of $Pb_2P_2Se_6$ within the sX-LDA scheme and b) projected partial density of states (PDOS) of Pb, c) P, and d) Se.

In terms of the detector performance, the $Pb_2P_2Se_6$ compound is still at a very early stage of development. It has to be noted that the crystallinity and purity of the $Pb_2P_2Se_6$ samples can vary depending on their position in a multi-centimeter long crystal ingot. In general, the tip part (first to solidify) of a Bridgman-grown crystal ingot exhibited lower crystallinity due to the competition between multiple seeds. The heel portion (last to solidify) of the same crystal ingot, on the other hand, retained more impurities. As a result, the spectroscopic performances of the extracted single crystal samples depended on their positions along the ingot. We find that $Pb_2P_2Se_6$ samples can exhibit spectroscopic responses under γ-radiation (**Figure 6**a), with resolvable spectroscopic features. Figure 6b presents two pulse height spectra of ^{57}Co γ-radiation generated by a $Pb_2P_2Se_6$ single crystal wafer at 600 (top) and 800 V (bottom) bias. At 600 V, the $Pb_2P_2Se_6$ wafer produced a ^{57}Co γ-ray spectrum with resolved features that are comparable to those in a CZT-generated spectrum (Figure 6b, gray spectrum). At an increased bias of 800 V, the spectrum from the same $Pb_2P_2Se_6$ sample became more convoluted, while a shift of peak maxima (position in detector channel number) can be observed, elucidating the sample's response to the change in bias voltage.

In addition to these responses, several $Pb_2P_2Se_6$ crystals were able to generate partially resolved ^{57}Co γ-ray spectra. Figure 6c,d demonstrates two pulse height of a ^{57}Co source which emits 14.4, 122.1, and 136.5 keV γ-rays with relative intensities of 0.11, 1, and 0.12, respectively. The spectrum in Figure 6c shows two major peaks matching the 122.1 and

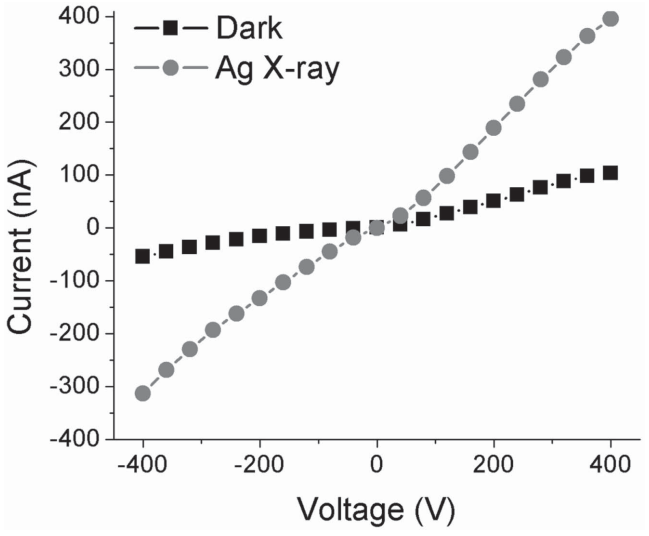

Figure 5. Electrical resistivity of $Pb_2P_2Se_6$ with (gray) and without (black) Ag X-ray.

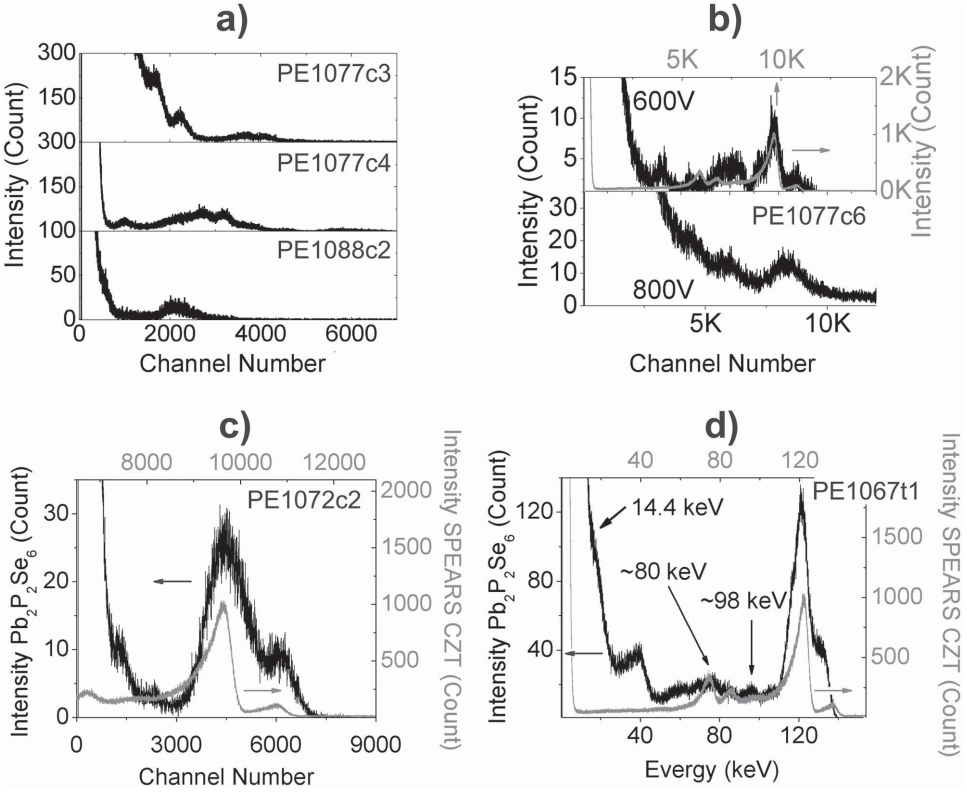

Figure 6. a) Unresolved ^{57}Co γ-ray spectroscopic responses of the $Pb_2P_2Se_6$ crystal samples. b) ^{57}Co γ-ray spectroscopic responses of a $Pb_2P_2Se_6$ single crystal wafer at 600 and 800 V bias compared to that of a SPEARS CZT detector (gray spectrum). c,d) Partially resolved ^{57}Co γ-ray spectra of $Pb_2P_2Se_6$ crystals compared with that of a SPEAR detector (CZT).

136.5 keV lines of the ^{57}Co spectrum from CZT, while other minor features were too weak to be identified. In Figure 6d, the $Pb_2P_2Se_6$ sample resolved the main peak at 122.1 keV with a resolution of ≈10 keV FWHM. Due to the relatively low resolution, the 136.5 keV radiation was only partially resolved as a shoulder of the 122.1 keV signal. The typical Compton scattering feature at ≈80 keV was also recorded and found matching those recorded by typical CZT detectors.[19] The small peak at ≈98 keV could be attributed to the Pb atom escape line, which is intrinsic to the composition. The broad peak between 30 and 40 keV is believed to be related to a breakdown current formed under the large electric field, which also contributes to the high background at low energy. We believe the 14.4 keV γ-radiation signal is convoluted with the large background forming a broad shoulder feature.

The spectroscopic response at different applied voltages allowed us to evaluate the mobility–lifetime products of electron carriers using a methodology developed by Ruzin and Nemirovsky,[20] which employs a modified Hecht equation[21] (Equation (1)). This method is based on spectroscopy measurements of the X-ray or γ-ray photons. The mobility–lifetime products for electrons is derived from the analysis of the maximal charge collection efficiency (CCE) under each bias voltage applied to the sample, specifically, the channel location that has the maximum photon counts under a given bias voltage. By varying the applied bias voltage V, the maximum response count channel $Ch(V)$ varies accordingly. The CCE is linked to parameter V, the bias voltage applied to the sample as

$$\mathrm{CCE}(V) = \frac{Ch(V)}{\mathrm{const}} = \frac{\mu\tau V}{L^2}\left[1 - e^{-\frac{L^2}{\mu\tau V}}\right] \quad (1)$$

where L (0.171 cm) is the thickness of the sample. With negative bias applied to the surface facing the radiation source, electron carriers were collected and the maximum response count channel under the 122.1 keV characteristic peak was recorded. By using the maximum centroid channel numbers $Ch1$ (9910) and $Ch2$ (12747) under the two bias voltages, $V1$ = 400 V, and $V2$ = 600 V, and Equation (1), the estimated lifetime–mobility product of the sample is 3.5×10^{-5} cm^2 V^{-1} for electron carriers. Multiplied by the applied external electric field under 600 V bias, 600 V/0.171 cm = 3509 V cm^{-1}, the drift length is estimated to be 1.23 mm under 600 V bias. Under 400 V bias, it is estimated to be 0.82 mm. The parameter "const" is the maximum channel corresponding to the limit reachable, estimated to be 23 618. We have tested this method by measuring a CZT sample under a ^{57}Co radiation source. The mobility–lifetime product for electron carriers of the CZT sample ($4 \times 4 \times 2$ mm^3, eV Products) was measured using the same method. Two bias voltages, 200 and 300 V, were used. The value was estimated to be 5.8×10^{-3} cm^2 V^{-1}, which is in good agreement with previous measurements.

3. Conclusion

The heavy metal chalcophosphate, $Pb_2P_2Se_6$, is a promising semiconductor for X-ray/γ-ray detector. Here, procedures for bulk synthesis, crystal growth, and sample processing have been described. Large single crystals of $Pb_2P_2Se_6$ with high resistivity were grown by vertical Bridgman method, which were subsequently waferized and processed for physical property measurements and γ-ray detector testing. The optical bandgap of bulk $Pb_2P_2Se_6$ is 1.88 eV, and is indirect in nature as indicated by the electronic structure calculations. The $Pb_2P_2Se_6$ crystal samples exhibited relatively low mobility–lifetime products, but despite this, they exhibited good photocurrent response toward 40 keV Ag X-ray and were able to produce a resolved ^{57}Co γ-ray spectrum.

The $Pb_2P_2Se_6$ compound is a promising cost-effective hard radiation detector material because of its robust chemical and physical properties. The availability and stability of the starting materials should allow the simpler preparation of functioning detector samples. Its thermal behavior implies less technological and engineering challenges in terms of crystal growth and scale up. Finally, the good mechanical hardness of $Pb_2P_2Se_6$ promises easy adaption to existing post-growth processes and detector fabrication techniques. Of course further improvements are needed in crystal quality, and higher mobility–lifetime products can be achieved from continued refinement of the crystal growth process.

4. Experimental Section

Synthesis and Crystal Growth: Polycrystalline samples of $Pb_2P_2Se_6$ were prepared from lead metal (rod, Alfa Aesar, various purity), selenium (shots, Alfa Aesar, various purity), and red phosphorous (pieces, Alfa Aesar, various purity). During the sample preparation, lead metal was etched with 5% HNO_3 solution, then rinsed with pure ethanol in order to remove the surface oxide. 60 g of stoichiometric starting materials were loaded into tapered fused silica ampoules (13 mm ID, 1 mm wall thickness, and 200 mm in length) and sealed under vacuum ($\approx 10^{-4}$ Torr). The samples were heated to 950 °C over 72 h and held at the maximum temperature for 12 h before they were cooled to room temperature over 12 h. The as-obtained polycrystalline samples, with their original silica ampoules intact, were subsequently used for single crystal growth in a modified vertical two-zone Bridgman furnace equipped with a geared dropping mechanism. The temperature of the hot zone was 850 °C, while the cold zone was 650 °C. The crystal growth was carried out with a lowering rate of 0.5 mm h^{-1}. Once the samples were completely lowered into the cold zone, they were annealed in situ at 650 °C for 24 h. Finally, the grown crystals were cooled to room temperature over 24 h. The temperature gradient in the two-zone Bridgman furnace was estimated to be 30 °C cm^{-1}. Segmented crystal ingots were obtained from the crystal growth. The solid crystal ingots naturally fracture in the direction perpendicular to the thermal gradient, forming smaller segments toward the tip of the tapered ampoule and largest segments (up to 25 mm long) at the heel part. The compositions and phase purity of the $Pb_2P_2Se_6$ crystals were verified by powder X-ray diffraction (Figure S8, Supporting Information).

X-Ray Diffraction Studies: X-ray powder diffraction experiments were conducted on a silicon-calibrated CPS 120 Inel powder X-ray diffractometer with CuKα1 radiation. The data were collected in an angular range of 0°–120° 2θ with a scan step 0.029°. Experimental powder XRD patterns were compared to the simulated diffraction pattern based on the reported single crystal structure.[9] The powder XRD patterns showed good agreement with the calculated XRD patterns from the single crystal models. To verify the crystal structure, single crystal X-ray diffraction was performed at 298(2) K on extracted $Pb_2P_2Se_6$ single crystals with a Stoe image plate diffraction system (IPDS) II diffractometer using graphite-monochromated MoKα radiation (λ = 0.71073). Data process and numerical absorption corrections were performed using Stoe X-Area software.[22] Structures were solved by direct methods and refined by full-matrix least-squares on F^2 (all data) using the SHELXTL software suite.[23] The crystallographic and structural information is summarized in Tables S1–S3, Supporting Information.

Waferization and Polishing: The larger $Pb_2P_2Se_6$ crystal segments were cut into wafers of 1–2 mm thick in perpendicular to the growth direction using a Struers Accutom-50 waferizing saw equipped with a 300 µm wide diamond-impregnated blade. The sample surface was polished by hand with successively finer grit SiC grinding papers down to 3 µm particle size. Then the fine polishing was achieved mechanically with 0.05 µm suspended Al_2O_3 slurry. After polishing, the processed $Pb_2P_2Se_6$ crystals exhibited mirror like smooth surfaces. The processed samples were usually irregular shaped due to fracturing occurred during polishing. The average surface area of the wafers ranged from 3 × 3 up to 5 × 10 mm, while the thickness varied between 1 and 2 mm.

Differential Thermal Analysis: DTA were performed on a Shimadzu DTA-50 thermal analyzer. Around 20 mg of ground crystalline samples were sealed in a fused silica ampoule under vacuum. A similar amount of α-Al_2O_3 powder sealed in a separated ampoule was used as a reference. The samples were heated and cooled to a maximum temperature of 900 °C. A heating/cooling rate of 5 °C min^{-1} was used up to 600 °C, while a slower rate of 1 °C min^{-1} was used between 600 and 900 °C. The melting and crystallization points were taken as the temperatures of the endothermic and exothermic peaks, respectively.

Optical Characterization: In order to determine the optical bandgap of $Pb_2P_2Se_6$, optical diffuse reflectance measurements were employed. The measurements were performed at room temperature using a Shimadzu UV-3101-PC double-beam, double-monochromator spectrophotometer. Data were collected in the range of 200–2500 nm with $BaSO_4$ as a 100% reflectance standard. The finely ground crystalline sample was spread on a compacted substrate of $BaSO_4$ powder. The generated reflectance versus wavelength data were converted to absorbance data using the Kubelka–Munk equation so the optical bandgap can be estimated.[24]

Thermal Conductivity: A selected single crystal wafer (6 × 6 × 2 mm) was subjected to thermal conductivity measurement. A thin layer of graphite coating was applied to the sample to minimize errors from the emissivity of the material. Total thermal conductivity, κ, was calculated using the following equation

$$k = \alpha C_p d \tag{2}$$

where α, C_p, and d are the thermal diffusivity coefficient, the specific heat, and the density, respectively. The thermal diffusivity coefficient (α) was measured using the laser flash diffusivity method in a Netzsch LFA457 Laser Flash Apparatus, while the specific heat capacity (C_p) of $Pb_2P_2Se_6$ was indirectly derived using a standard (Pyroceram 9606) in the range of 300–673 K. A Cowan model with pulse correction was applied to the analysis of the thermal diffusivity data, where cooling cycles gave reproducible values for each sample.

Hardness Measurements: A $Pb_2P_2Se_6$ single crystal was analyzed via the microindentation measurements using a Struers Duramin 5 automated micro hardness tester equipped with a Knoop tip. Indentations were made with a 25 g load for 5 s at random locations on the surface of a fine-polished $Pb_2P_2Se_6$ crystal wafer. The indentations were subsequently evaluated using a calibrated, built-in high-resolution microscope to extract the Knoop hardness[25] values for each indentation trace.

Transport and Detector Property Measurements: Direct current resistivity was measured in the dark using a Keithley 6517b electrometer. Colloidal graphite paint was used to connect copper wires to the surfaces of the $Pb_2P_2Se_6$ wafer samples. During the measurements, the voltage was swept from −400 to 400 V with a dwell time of 30 s. Photoconductivity was measured in parallel with

an Ag X-ray tube source (40 kV, 10 mA) illuminating the sample. For the detector property measurement, $Pb_2P_2Se_6$ single crystal wafers 1–2 mm thick were exposed to a 1.0 mCi ^{57}Co source. In each measurement, the sample was placed in an eV-480 test fixture which is connected to an eV-550 preamplifier box. A positive bias between 400 and 800 V was applied to a crystal wafer to maintain an electric field up to $\approx 8 \times 10^5$ V m^{-1}. A SPEAR detector with a $5 \times 5 \times 5$ mm CZT crystal was used as a reference and it was operated at a bias voltage of 1000 V. For the $Pb_2P_2Se_6$ samples, the signals were transferred to an ORTEC amplifier (Model 572A) with a gain of 200–1000 and shaping time of 0.5–6 μs, while the signal from the commercial CZT detector was amplified with a gain of 1000 and shaping time of 0.5 μs. The processed signals were subsequently evaluated by a dual 16 K input multichannel analyzer (Model ASPEC-927) and read into the MAESTRO-32 software. The detailed measurement parameters are summarized in Table S4 (Supporting Information), with respect to the spectra in Figure 6.

Electronic Structure Calculations: The electronic band structure of $Pb_2P_2Se_6$ was determined using the projector augmented wave method[26] as implemented in the Vienna ab initio Simulation Package.[27] Energy cutoff for the plane wave basis was set to 350 eV and the $5 \times 5 \times 3$ Monkhorst–Pack grid was used for momentum space integrations in a self-consistent calculation.[28] In order to predict a bandgap correctly, the hybrid functional was employed within the Heyd–Scuseria–Ernzerhof formalism.[29] Spin–orbit coupling was included in a noncollinear scheme.

Supporting Information

Supporting Information is available from the Wiley Online Library or from the author.

Acknowledgements

This work was supported by the Department of Homeland Security ARI program with Grant No. 2014-DN-077-ARI086-01. Hardness measurements were performed at the Optical Microscopy and Metallography Facility at Northwestern University. The X-ray photoconductivity measurement was performed with the help of Dr. Christos Malliakas. Refined electronic structure calculation was performed by Dr. Oleg Kontsevoi.

Received: May 3, 2015
Revised: June 6, 2015
Published online: July 2, 2015

[1] a) A. Owens, *J. Synchrotron Radiat.* **2006**, *13*, 143; b) A. Owens, A. Peacock, *Nucl. Instrum. Methods Phys. Res., Sect. A* **2004**, *531*, 18.
[2] J. Androulakis, S. C. Peter, H. Li, C. D. Malliakas, J. A. Peters, Z. Liu, B. W. Wessels, J.-H. Song, H. Jin, A. J. Freeman, M. G. Kanatzidis, *Adv. Mater.* **2011**, *23*, 4163.
[3] a) M. R. Squillante, W. M. Higgins, H. Kim, L. Cirignano, G. Ciampi, A. Churilov, K. Shah, *Proc. SPIE* **2009**, *7449*, 74491U; b) G. A. Samara, *Phys. Rev. B: Condens. Matter Mater. Phys.* **1981**, *23*, 575.
[4] H. Chen, S. A. Awadalla, J. Mackenzie, R. Redden, G. Bindley, A. E. Bolotnikov, G. S. Camarda, G. Carini, *IEEE Trans. Nucl. Sci.* **2007**, *54*, 811.
[5] a) S. Johnsen, Z. Liu, J. A. Peters, J.-H. Song, S. Nguyen, C. D. Malliakas, H. Jin, A. J. Freeman, B. W. Wessels, M. G. Kanatzidis, *J. Am. Chem. Soc.* **2011**, *133*, 10030; b) S. Johnsen, Z. Liu, J. A. Peters, J.-H. Song, S. C. Peter, C. D. Malliakas, N. K. Cho, H. Jin, A. J. Freeman, B. W. Wessels, M. G. Kanatzidis, *Chem. Mater.* **2011**, *23*, 3120; c) H. Li, C. D. Malliakas, Z. Liu, J. A. Peters, H. Jin, C. D. Morris, L. Zhao, B. W. Wessels, A. J. Freeman, M. G. Kanatzidis, *Chem. Mater.* **2012**, *24*, 4434; d) H. Li, C. D. Malliakas, J. A. Peters, Z. Liu, J. Im, H. Jin, C. D. Morris, L.-D. Zhao, B. W. Wessels, A. J. Freeman, M. G. Kanatzidis, *Chem. Mater.* **2013**, *25*, 2089; e) H. Li, J. A. Peters, Z. Liu, M. Sebastian, C. D. Malliakas, J. Androulakis, L. Zhao, I. Chung, S. L. Nguyen, S. Johnsen, B. W. Wessels, M. G. Kanatzidis, *Cryst. Growth Des.* **2012**, *12*, 3250; f) S. L. Nguyen, C. D. Malliakas, J. A. Peters, Z. Liu, J. Im, L.-D. Zhao, M. Sebastian, H. Jin, H. Li, S. Johnsen, B. W. Wessels, A. J. Freeman, M. G. Kanatzidis, *Chem. Mater.* **2013**, *25*, 2868; g) S. Wang, Z. Liu, J. A. Peters, M. Sebastian, S. L. Nguyen, C. D. Malliakas, C. C. Stoumpos, J. Im, A. J. Freeman, B. W. Wessels, M. G. Kanatzidis, *Cryst. Growth Des.* **2014**, *14*, 2401; h) A. C. Wibowo, C. D. Malliakas, D. Y. Chung, J. Im, A. J. Freeman, M. G. Kanatzidis, *Inorg. Chem.* **2013**, *52*, 2973; i) A. C. Wibowo, C. D. Malliakas, D. Y. Chung, J. Im, A. J. Freeman, M. G. Kanatzidis, *Inorg. Chem.* **2013**, *52*, 11875; j) A. C. Wibowo, C. D. Malliakas, Z. Liu, J. A. Peters, M. Sebastian, D. Y. Chung, B. W. Wessels, M. G. Kanatzidis, *Inorg. Chem.* **2013**, *52*, 7045.
[6] a) E. A. Axtell, J.-H. Liao, Z. Pikramenou, M. G. Kanatzidis, *Chem. Eur. J.* **1996**, *2*, 656; b) E. A. Axtell, Y. Park, K. Chondroudis, M. G. Kanatzidis, *J. Am. Chem. Soc.* **1998**, *120*, 124; c) E. G. Tulsky, J. R. Long, *Chem. Mater.* **2001**, *13*, 1149.
[7] a) S. Banerjee, C. D. Malliakas, M. G. Kanatzidis, *Inorg. Chem.* **2012**, *51*, 11562; b) I. Chung, K. Biswas, J.-H. Song, J. Androulakis, K. Chondroudis, K. M. Paraskevopoulos, A. J. Freeman, M. G. Kanatzidis, *Angew. Chem., Int. Ed.* **2011**, *50*, 8834; c) I. Chung, M. G. Kanatzidis, *Inorg. Chem.* **2011**, *50*, 412; d) M. A. Gave, D. Bilc, S. D. Mahanti, J. D. Breshears, M. G. Kanatzidis, *Inorg. Chem.* **2005**, *44*, 5293; e) M. A. Gave, C. D. Malliakas, D. P. Weliky, M. G. Kanatzidis, *Inorg. Chem.* **2007**, *46*, 3632; f) C. D. Morris, M. G. Kanatzidis, *Inorg. Chem.* **2010**, *49*, 9049; g) A. Rothenberger, H.-H. Wang, D. Chung, M. G. Kanatzidis, *Inorg. Chem.* **2010**, *49*, 1144; h) T. J. McCarthy, M. G. Kanatzidis, *Inorg. Chem.***1995**, *34*, 1257. i) K. Chondroudis, T. J. McCarthy, M. G. Kanatzidis, *Inorg. Chem.* **1996**, *35*, 840.
[8] C. D. Carpenti, R. Nitsche, *Mater. Res. Bull.* **1974**, *9*, 401.
[9] H. Yun, J. A. Ibers, *Acta Crystallogr. Sect. C: Cryst. Struct. Commun.* **1987**, *43*, 2002.
[10] S. M. Seltzer, *Radiat. Res.* **1993**, *136*, 147.
[11] A. Owens, *Compound Semiconductor Radiation Detectors*, CRC Press, **2012**.
[12] I. P. Prits, M. V. Potorij, Y. V. Voroshilov, *Ukr. Khim. Zh.* **1989**, *55*, 135.
[13] a) I. Martynyuk-Lototska, O. Mys, B. Zapeka, M. Kostyrko, A. Grabar, R. Vlokh, *Appl. Opt.* **2014**, *53*, B103; b) O. Mys, I. Martynyuk-Lototska, A. M. Kostruba, A. Grabar, R. Vlokh, *Ukr. J. Phys. Opt.* **2012**, *13*, 177.
[14] V. M. Rizak, K. Al'-Shoufi, I. M. Rizak, I. P. Prits, Y. M. Vysochanskii, V. Y. Slivka, *Ferroelectrics* **1994**, *155*, 323.
[15] M. E. Rodríguez, J. J. Alvarado-Gil, I. Delgadillo, O. Zelaya, H. Vargas, F. Sánchez-Sinencio, M. Tufiño-Velázquez, L. Baños, *Phys. Status Solidi A* **1996**, *158*, 67.
[16] R. J. Gummow, I. Sigalas, *Int. J. Thermophys.* **1987**, *8*, 607.
[17] S. Adachi, *Properties of Group-IV, III-V and II-VI Semiconductors*, Wiley, **2005**.
[18] A. V. Churilov, G. Ciampi, H. Kim, W. M. Higgins, L. J. Cirignano, F. Olschner, V. Biteman, M. Minchello, K. S. Shah, *J. Cryst. Growth* **2010**, *312*, 1221.
[19] G. R. Gilmore, *Practical Gamma-Ray Spectrometry*, Wiley, **2008**.
[20] A. Ruzin, Y. Nemirovsky, *J. Appl. Phys.* **1997**, *82*, 4166.
[21] K. Hecht, *Z. Phys.* **1932**, *77*, 235.

[22] STOE & Cie GmbH, Darmstadt, **2006**.
[23] G. M. Sheldrick, University of Göttingen, Göttingen, Germany **1997**.
[24] S. P. Tandon, J. P. Gupta, *Phys. Status Solidi B* **1970**, *38*, 363.
[25] F. Knoop, C. G. Peters, W. B. Emerson, *J. Res. Natl. Bur. Stand.* **1939**, *23*, 39.
[26] P. E. Blöchl, *Phys. Rev. B: Condens. Matter Mater. Phys.* **1994**, *50*, 17953.
[27] a) G. Kresse, J. Hafner, *Phys. Rev. B: Condens. Matter Mater. Phys.* **1993**, *47*, 558; b) G. Kresse, J. Furthmüller, *Phys. Rev. B* **1996**, *54*, 11169.
[28] H. J. Monkhorst, J. D. Pack, *Phys. Rev. B: Condens. Matter Mater. Phys.* **1976**, *13*, 5188.
[29] J. Heyd, G. E. Scuseria, M. Ernzerhof, *J. Chem. Phys.* **2003**, *118*, 8207.